ACS APPLIED ENERGY MATERIALS

www.acsaem.org

Article

Rational Engineering of Amide-Based Electrolytes for "True"-Lithium−Air Batteries Working by Atmospheric Oxygen

Published as part of ACS Applied Energy Materials special issue "Material and Interface Design in Next-Generation Batteries".

Akihiro Nomura,* Shota Azuma, Fumisato Ozawa, and Morihiro Saito

Cite This: ACS Appl. Energy Mater. 2026, 9, 827−841

Read Online

ABSTRACT: Lithium−air batteries (LABs) offer ultrahigh energy density, but their practical use is limited by the sluggish oxygen reduction reaction, which requires operation under pure oxygen and yields extremely low power output. Herein, to boost both the power and energy under air oxygen, we investigated the discharge performance of LAB cells with low-viscosity amide-based electrolytes, *N*,*N*-dimethylacetamide (DMA) and *N*,*N*-dimethylformamide (DMF), dissolving lithium nitrate ($LiNO_3$) or lithium bis(trifluloromethanesulfonyl)imide (LiTFSI). With viscosities $^1/_3$−$^1/_4$ lower than that of the typical LAB solvent of tetraethylene glycol dimethyl ether (TEG), the amide-based electrolytes ensure rapid transport of oxygen and Li^+ ions, thereby enhancing battery output. Raman spectroscopy revealed that $LiNO_3$-based electrolytes exhibit weaker solvation, explaining their lower viscosity with slightly reduced ionic conductivity compared to LiTFSI-based electrolytes, with this effect more evident in DMF. As a result, LAB cells with DMF electrolyte dissolving 1.0 M $LiNO_3$ (DMF-NO_3) achieved the highest current density discharge of 23 mA cm^{-2} with a capacity of 2.2 mAh cm^{-2} under dry air, corresponding to an "engine-like" power of 2200 W kg^{-1} and an energy density of 210 Wh kg_{energy}^{-1}. Galvanostatic discharge−charge cycling tests revealed better cyclability for DMA-based electrolytes due to reduced solvent volatilization. Anion mixing further suppressed the solvent loss and minimized side reactions, providing 200 Wh kg_{energy}^{-1} over 14 cycles. Due to the milder oxidative conditions, LAB cells increased the rechargeability under dry air rather than under pure oxygen. This work paves the way for the development of "true" LABs capable of operating efficiently using atmospheric oxygen.

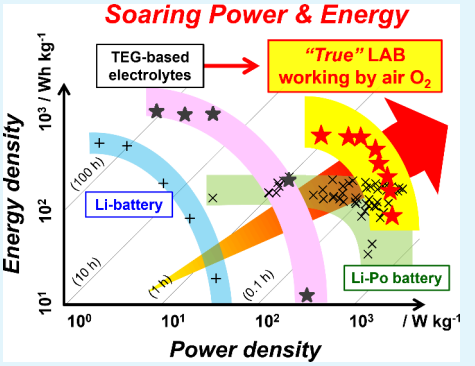

KEYWORDS: *lithium−air battery, amide-based electrolyte, solvation, atmospheric oxygen, highly porous cathode, high power density, high energy density*

1. INTRODUCTION

Lithium−air battery (LAB) is a battery technology that generates electric power by the air oxidation of lithium, achieving high gravimetric energy density beyond lithium-ion battery (LiB). Due to the recent progress of the battery materials and cell assembling technology, Ah-class LAB cells with gravimetric energy densities exceeding the high-energy density criteria of 500 Wh kg^{-1} have been reported.[1−3] Despite this, the poor power output makes practical applications difficult. Due to the sluggish battery reaction, LABs require a pure O_2 gas environment for discharge. Because atmospheric O_2 (~21%) severely worsens the discharge performance,[4] the present LAB technology is not strictly relevant to "air" batteries. Most LAB studies have conducted research in a pure O_2 gas environment, referring to their systems as "Li−O_2" rather than "Li−air". This approach is, of course, important for deriving scientific results under controlled conditions, but the results could be irrelevant to the practical battery performance as an "air" battery.

For practical applications, LABs need to operate under atmospheric O_2 rather than a pure O_2 environment. To this end, researchers have sought to enhance the battery reaction rate by incorporating oxygen redox catalysts. Inorganic solid catalysts supported on the cathode surface reduce the overpotential and improve the discharge−charge performance,[5,6] but such catalysts simultaneously accelerate electrolyte and electrode degradation. Redox mediators are also effective in reducing the battery overpotential,[7−11] although they can induce self-discharge (shuttle effect) and lithium anode corrosion. Perfluorocarbons in liquid electrolytes improve the discharge performance by increasing the soluble O_2 concen-

Received: September 24, 2025
Revised: December 30, 2025
Accepted: January 2, 2026
Published: January 10, 2026

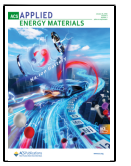

https://doi.org/10.1021/acsaem.5c02972
ACS Appl. Energy Mater. 2026, 9, 827−841

tration, but they also suffer from fast degradation.[12−14] Because such additives must be loaded in substantial amounts to be effective, they diminish the lightweight nature of LABs with increasing material cost. Their practical availability in LAB systems remains controversial.

Air electrode (the cathode of air battery) plays a crucial role in the battery reaction process, i.e., oxygen reduction/evolution reactions (ORR/OER), specifically $2Li^+ + 2e^- + O_2 \leftrightarrow Li_2O_2$ for LABs. Continuous deposition of lithium peroxide (Li_2O_2) during discharge requires the cathode to have a high surface area to ensure fast ORR/OER, along with plentiful mesopores to adsorb oxygen and cultivate the discharge product.[15−20] Recent reports indicate that the integrated cathode pore architecture has more impact on the current capability,[21−24] by ensuring efficient O_2 diffusion across the cathode and enabling higher current rate discharge. While most LAB studies report a battery performance at a current density below 0.5 mA cm^{-2}, we have recently succeeded in increasing the discharge current to 3.0 mA cm^{-2} by using highly porous carbon nanotube (CNT) sheet cathodes with porosities of up to 95%.[25] This current rate capability can be further enhanced to 5.0 mA cm^{-2}, securing a capacity of 4.3 mAh cm^{-2} in atmospheric O_2 conditions, by combining the porous CNT cathode with an *N*-methylpyrrolidone (NMP)-based low-viscosity amide-based electrolyte, which facilitates smooth O_2 transport and achieves unprecedented power improvement.[26]

The rising power under atmospheric oxygen dioxide (O_2) encourages the development of "true" LABs that are capable of operating under atmospheric air. This trend poses a new need for fundamental studies of the ORR/OER processes at low O_2 concentrations, including systematic investigations of the cell performance under atmospheric O_2 and the rational engineering of battery materials. To this end, this study investigates the discharge power and cycling performance of LAB cells with amide-based electrolytes under dry air. Along with tetraethylene glycol dimethyl ether (TEG), amides are also known as potential LAB electrolyte solvents that allow reversible Li_2O_2 deposition and decomposition.[27−30] To achieve high power performance, low-viscosity amide-based electrolytes of *N*,*N*-dimethylacetamide (DMA) and *N*,*N*-dimethylformamide (DMF) dissolving lithium nitrate ($LiNO_3$) or lithium bis(trifluoromethanesulfonyl)imide (LiTFSI) (Figure 1) were combined with the highly porous CNT sheet cathodes. The viscosities of DMA and DMF are approximately $^1/_3$−$^1/_4$ that of TEG, enabling high electrolyte fluidity (Table S1). Among the prepared electrolytes, DMF-based electrolyte dissolving 1.0 M $LiNO_3$ (DMF-NO_3) exhibited the lowest viscosity with high ionic conductivity, attaining a record-high current rate capability of 23 mA cm^{-2}, while securing a high discharge capacity of 2.2 mAh cm^{-2}. This demonstrates an engine-like power output of 2200 W kg^{-1} and delivers an energy of 210 Wh kg^{-1}, with respect to the battery material weight. Meanwhile, a DMA-based electrolyte containing the mixed anions of $TFSI^-$ and NO_3^- attained the best cyclability, providing 200 Wh kg_{energy}^{-1} for 14 cycles thanks to reduced side reactions and suppressed solvent vaporization. This study sets a new paradigm for developing "true" LABs capable of operating under atmospheric air for powering electronic mobilities.

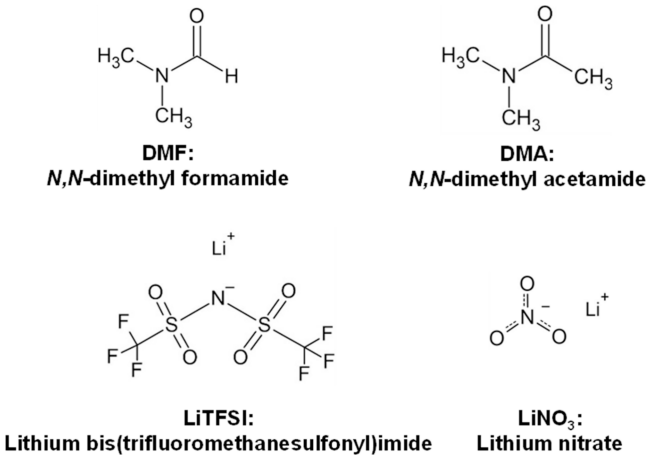

Figure 1. Electrolyte solvents and salts used in this study.

2. EXPERIMENTAL SECTION

2.1. Materials

$LiNO_3$ (99.0%, Kishida Chemical) and LiTFSI (99.95%, Kishida Chemical) were dehydrated overnight at 110 °C under vacuum before being dissolved in DMF (superdehydrated grade, Fujifilm Wako Chemicals) or DMA (superdehydrated grade, Fujifilm Wako Chemicals). The resulting electrolytes were labeled as X−Y, where X indicates the solvent and Y refers to the salt anion. The H_2O content, measured using a Karl Fischer moisture meter (CA-31, Mitsubishi Chemical Corp.), was approximately 150 ppm across all electrolytes. Single-walled CNTs (ZEONANO SG101, Sigma-Aldrich) were dispersed in deionized water at a concentration of 0.1 wt % using an ultrasonic homogenizer (450D, Branson). The slurry was then filtered through carbon paper (300 μm thick, Kureha Corp.) to obtain a CNT sheet cathode supported on carbon paper as a gas diffusion layer (GDL). The CNT loading was 2.1 mg cm^{-2}, and the CNT layer thickness was approximately 130 μm with a porosity of 87%. The cathode Brunauer−Emmett−Teller (BET) surface area was 910 m^2 g^{-1} per the CNT loading weight, determined by the nitrogen adsorption isotherm at 77 K (3FLEX, Micromeritics).

2.2. Cell Assembly and Battery Testing

A stack-type LAB cell (Figure S1) was fabricated by layering lithium foil (⌀ 16 mm, 2.0 cm^2 electrode area, 200 μm thickness, Honjo Metal), a porous polyolefin separator (⌀ 19.5 mm, 20 μm thickness), and a CNT sheet cathode supported on carbon paper GDL (⌀ 16 mm) between aluminum and copper foil tapes as current collectors. The separator and CNT cathode were impregnated with 24 μL of electrolyte, and the stack was fixed under a pressure of 118 kPa. For discharge−charge cycling tests, the cell stack was sealed in a CR2032 stainless coin cell case with a perforated mesh on the cathode side (50% aperture ratio, Hohsen Corp.) to suppress the electrolyte evaporation and enable long-term testing (Figure S2). The electrolyte amount of 32 μL was injected into the coin cell. Galvanostatic discharge and charge were conducted using a battery tester (HJ1001SD8, Hokuto Denko) at room temperature in a dry room with an environmental dew point of approximately −60 to −50 °C (10−40 ppm of H_2O). The environmental O_2 and CO_2 gas concentrations were ca. 21% and <400 ppm, respectively. The discharge and charge cutoff voltages were set to 2.0 and 4.5 V, respectively. The cell weight during testing was monitored using a homemade gravimetric analysis system, described in the literature.[31] Gravimetric energy and power densities were calculated by dividing the cell energy and power by the total mass of the cell materials (60.6 mg for 200-μm-thick Li anode cells), respectively. The cell energy was obtained by integrating the discharge curve area (V-mAh) until a cutoff voltage of 2.0 V. The cell power is defined as the average discharge power obtained by dividing the discharge energy by the discharge time.

https://doi.org/10.1021/acsaem.5c02972
ACS Appl. Energy Mater. 2026, 9, 827−841

2.3. Characterization

Electrochemical impedance spectroscopy (EIS) measurements were conducted using an electrochemical measurement system (SP-200, BioLogic) in galvanostatic−EIS mode (GEIS, 50 mA amplitude) at 0.8 mA discharge (0.4 mA cm^{-2}) in the frequency range of 300 kHz to 100 mHz. The ionic conductivity and viscosity of the electrolytes were measured using a pH/ion meter (SevenExcellence S500, Mettler Toledo) and a rolling ball viscometer (Lovis2000ME, Anton Paar), respectively. The solvation structures of Li^+ in the electrolytes were evaluated using a laser Raman spectrometer (Raman Touch-Vis-NIR, Nanophoton) with a 532 nm excitation wavelength and a diffraction grating of 1200 gr/mm, providing a resolution to 1 cm^{-1}. Electrolyte anion analysis was conducted by using an ion chromatography system (ICS-2100, Dionex). Lithium anode and CNT cathode morphologies were analyzed by using field-emission scanning electron microscopy (SEM, JSM-7800F, JEOL, 5 keV accelerating voltage). X-ray diffraction (XRD) spectra of CNT cathodes after battery testing were recorded by a SmartLab X-ray diffractometer (Rigaku) with a Cu Kα source ($\lambda_{Cu\ K\alpha}$ = 1.524 Å).

3. RESULTS AND DISCUSSION

3.1. Physical Properties of Electrolytes

High-power LABs require smooth transport of the battery reactants, namely, O_2 and Li^+. To derive high current rates under atmospheric O_2, two low-viscosity amide solvents, DMA and DMF, which are both known to allow reversible Li_2O_2 deposition/decomposition,[28,30] were employed in this study. $LiNO_3$ and LiTFSI were dissolved as supporting salts to achieve the highest possible ionic conductivity in the resulting electrolytes. $LiNO_3$ is typically used as a supporting salt for amide-based electrolytes because the NO_3^- anion forms a thin oxide layer on a Li surface, serving as an effective solid−electrolyte interface (SEI) layer to suppress electrolyte decomposition and Li dendrite growth.[32,33] Meanwhile, LiTFSI is often used as an LAB electrolyte salt dissolved in TEG (TEG-TFSI) because of the noncoordinating nature of the $TFSI^-$ anion, which ensures high salt dissociation to provide high ionic conductivity.[34] Figure 2a shows the viscosity and ion conductivity of the electrolytes at 25 °C with varying salts concentrations (the raw data are tabulated in Table S1). In the graph (top), the viscosity values (η) were converted to fluidity (inverse of the viscosity, η^{-1}) because fluidity is an ideal measure of the diffusion coefficient (D) of transport species according to the Stokes−Einstein relationship $D = kT/\alpha\pi r\eta$, where k is the Boltzmann constant, T is the absolute temperature, α is a constant, and r represents the hydrodynamic radius of the diffusing species.[29] Decreasing the salt concentration monotonically increased the fluidity, approaching that of the pure solvent with near-zero ionic conductivity. Increasing the salt concentration raised the ion conductivity by increasing the number of carrier ions, maximizing around 1.0 M. Higher salt concentrations adversely decreased the ionic conductivity due to reduced electrolyte fluidity. This behavior is typical of many battery electrolytes[34] and was also observed in DMA- and DMF-based electrolytes dissolving $LiNO_3$ or LiTFSI. Of the two amide solvents, DMF provided higher ionic conductivity because of its lower molecular weight and hence lower viscosity (higher fluidity), which is important for achieving a high rate discharge, as discussed later. Between the two salts, LiTFSI gave higher ionic conductivity than $LiNO_3$ due to greater salt dissociation in the solvents, at the expense of higher viscosity (lower fluidity). LiTFSI-based electrolytes at concentrations of >1.0 M sharply decreased in conductivity due to excessive viscosity, hindering the smooth transport of Li^+ and O_2, which is detrimental to the battery power capability.

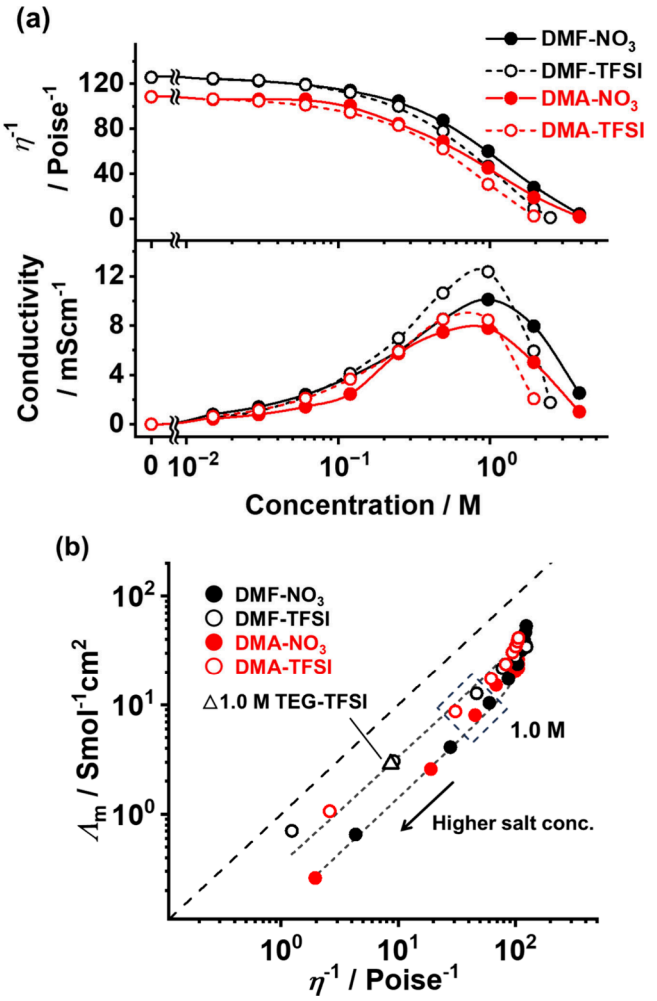

Figure 2. (a) Electrolyte fluidity (inverse of viscosity, η^{-1}, top) and ionic conductivity (bottom) plotted against the salt concentration. (b) Walden plot. Electrolyte molar conductivity values (Λ_m) were plotted against the electrolyte fluidity. The dashed straight line in the graph indicates values for a fully dissociated KCl aqueous solution.[35] The dotted lines are a visual guide to the trends of the data.

To further discuss the electrolyte behavior, the molar conductivity (Λ_m), derived by dividing the ionic conductivity by the molar concentration of salt (C_{Li}), is plotted against the fluidity (η^{-1}) in Figure 2b. The plot, known as the Walden plot, shows the relationship between ion dissociation and solvent mobility. The straight dashed line in the graph shows an ideal case of complete salt dissociation; an electrolyte closer to this line exhibits a higher degree of dissociation.[35] The data reveal that a low salt concentration renders the electrolytes high salt dissociation, with points closer to the ideal line. Increasing the salt concentration to ~0.50 M sharply decreases the Λ_m values, reducing the degree of dissociation. The linear relationship of Λ_m to η^{-1} for electrolytes above ~0.50 M indicates constant dissociation beyond this point, explaining the maximum ionic conductivity around 1.0 M. Between the two salts, LiTFSI presents higher salt dissociation, giving the linear relationship closer to the ideal line. For comparison, Figure 2b also includes a data point for 1.0 M TEG-TFSI (△), which is a common standard LAB electrolyte,[36−38] exhibiting nearly the same dissociation degree as DMF-TFSI

https://doi.org/10.1021/acsaem.5c02972
ACS Appl. Energy Mater. 2026, 9, 827−841

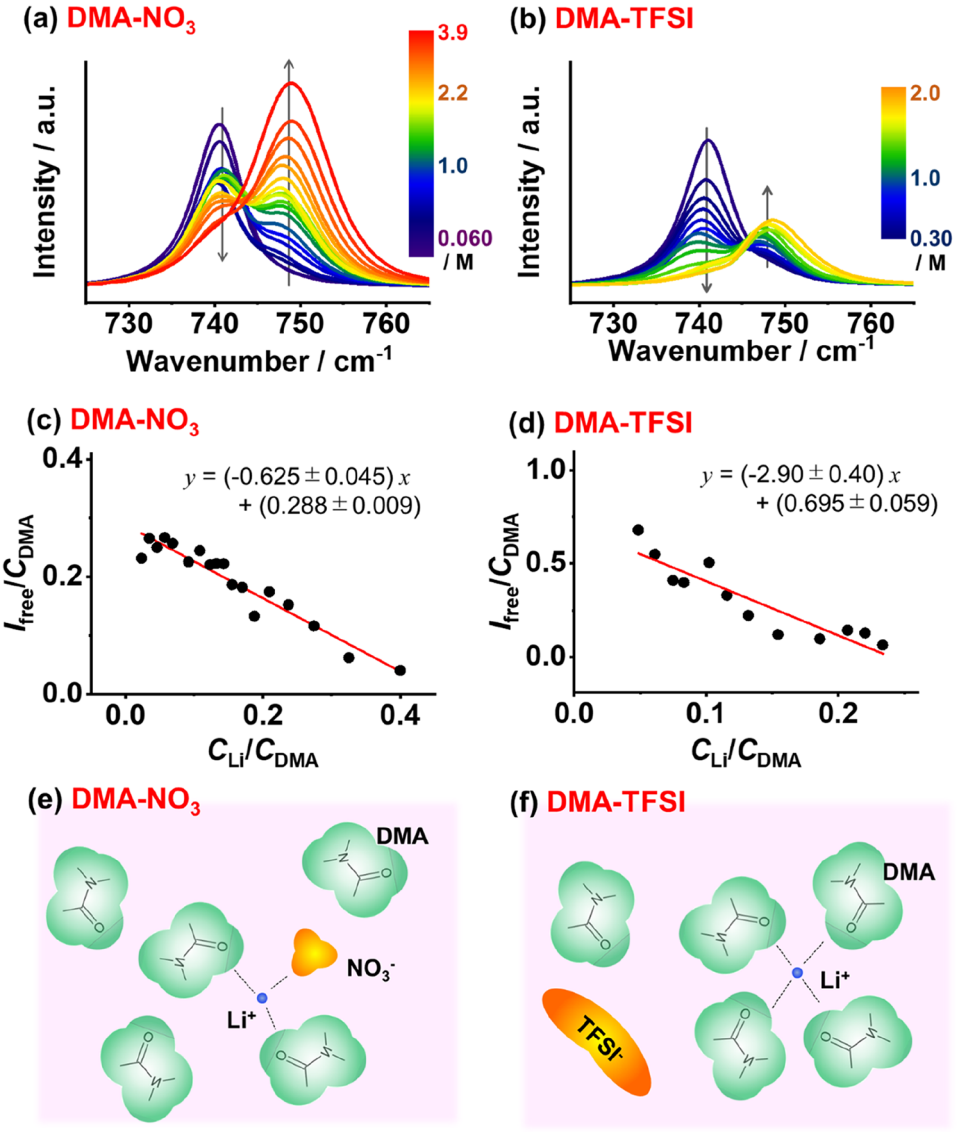

Figure 3. Raman spectra of DMA-NO_3 (a) and DMA-TFSI (b) electrolytes with varying salt concentrations. The arrow direction indicates the shift of the peak intensity along with increasing salt concentration. Plots of I_{free}/C_{DMA} vs C_{Li}/C_{DMA} for DMA-NO_3 (c) and DMA-TFSI (d) using the deconvoluted I_{free} band of 741 cm^{-1} for free DMA. The red straight lines indicate the linear fitting for the plotted data points. The equations in the graphs show the intercept and slope of the fitted lines, yielding the solvation numbers of 2.2 ± 0.2 and 4.2 ± 0.7 for DMA-NO_3 and DMA-TFSI, respectively. Schematic illustrations of the solvation structures for DMA-NO_3 (e) and DMA-TFSI (f). The Li^+ of DMA-NO_3 is solvated by two DMA molecules in contact with the NO_3^- anion, while the Li^+ of DMA-TFSI is solvated by four molecules with distance from the $TFSI^-$ anion.

and DMA-TFSI. However, its much lower fluidity compared to 1.0 M amide-based electrolytes fatally limits TEG-TFSI in high power applications. Among the 1.0 M amide-based electrolytes (data points in the dotted square region), fluidity followed the order of DMA-TFSI < DMA-NO_3, DMF-TFSI < DMA-NO_3, which correlates closely with the power capability discussed in the later section.

Solvation structures of the electrolytes were analyzed by Raman spectroscopy to investigate the origin of the electrolyte property. Parts a and b of Figure 3 show the Raman spectra of the DMA-NO_3 and DMA-TFSI electrolytes, respectively, with varying salt concentrations. The spectra for the DMF-based electrolytes are shown in Figure S3. The spectral peak intensity was calibrated by the Raman bands of NO_3^- (1042 cm^{-1})[39] or $TFSI^-$ (1246 cm^{-1})[40] anions, and the peak shown in Figure 3 is attributed to the $-N-CH_3$ stretching of a bulk DMA molecule (I_{free}, 741 cm^{-1}).[41] It should be noted that, because the Raman band of S−N−S stretching of a $TFSI^-$ anion appears at 744 cm^{-1},[40] the band was deducted for the DMA-TFSI spectra in Figure 3b to show the Raman intensity purely resulting from the $-N-CH_3$ stretching of DMA. The graph demonstrates that increasing the salt concentration decreases I_{free}, while another peak appears at 747 cm^{-1} and is ascribed to DMA molecule coordination to a Li^+ cation (I_{coord}). DMF-based electrolytes exhibited the same behavior, with a decrease in the Raman peak of $-N-CH_3$ stretching of 663 cm^{-1} (I_{free} of DMF) and an increase in another peak of 674 cm^{-1} (I_{coord} of DMF), along with an increase in the salt concentration (Figure S3).

The varying Raman intensity, depending on the salt concentration, allows us to estimate the number of solvent molecules coordinated to the Li^+ cation ($N_{solvent}$). The method is well explained elsewhere,[41,42] but, briefly, because I_{free} is expressed as $I_{free} = J_{free}C_{free}$, where J_{free} is the Raman scattering

https://doi.org/10.1021/acsaem.5c02972
ACS Appl. Energy Mater. 2026, 9, 827−841

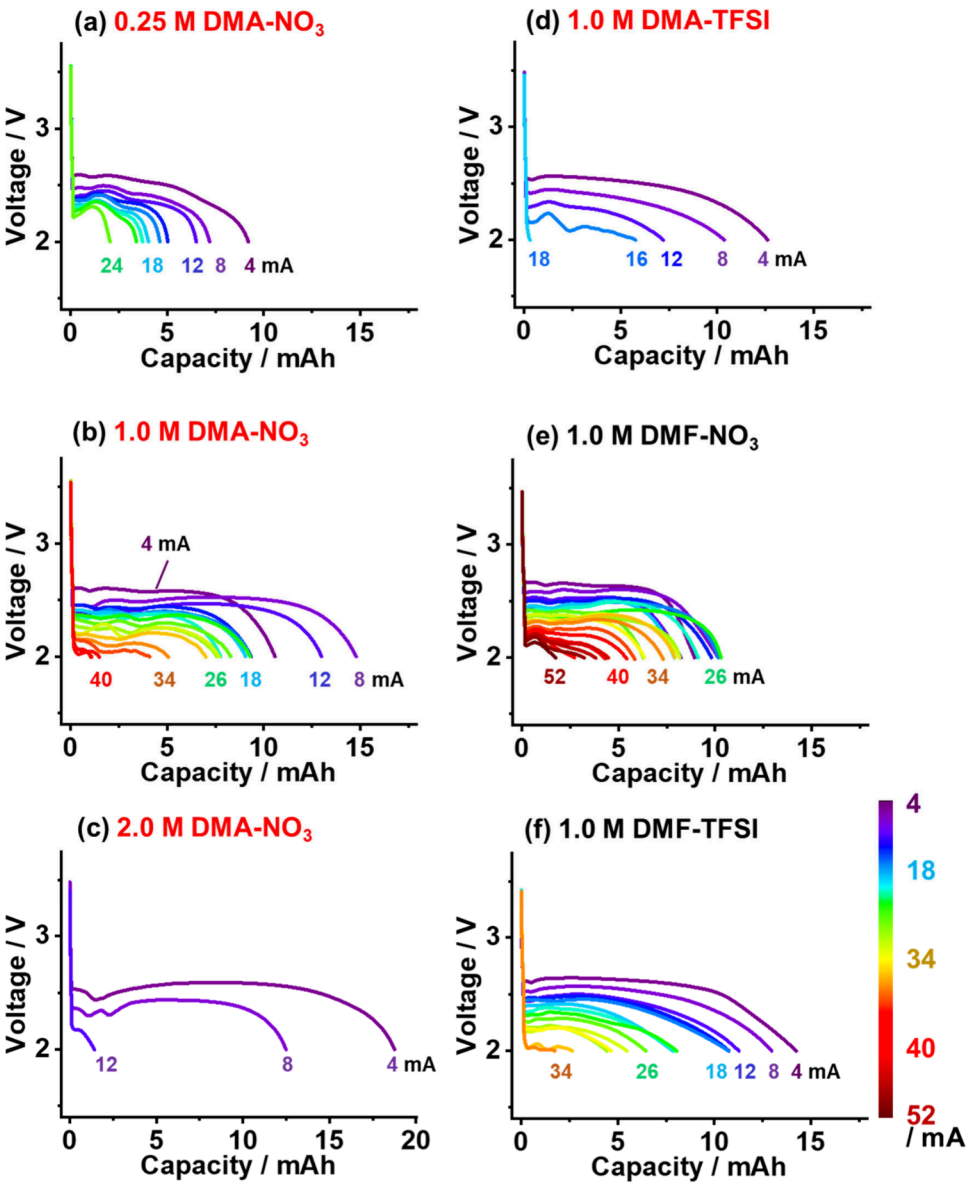

Figure 4. Discharge curves of stack-type LAB cells with 0.25 M (a), 1.0 M (b), and 2.0 M (c) DMA-NO_3 electrolyte. Discharge curves of stack-type LAB cells with 1.0 M DMA-TFSI (d), 1.0 M DMF-NO_3 (e), and 1.0 M DMF-TFSI (f). The numbers in the graphs indicate the applied current rates (mA). The highest capacity values achieved by three sets of cells at each rate condition were plotted.

coefficient of free bulk solvent and C_{free} refers to the molar concentration of the free bulk solvent, and C_{free} can be expressed as $C_{free} = C_{solvent} - N_{solvent}C_{Li}$, where $C_{solvent}$ represents the molar concentration of the total solvent, the two relationwhips give the following equation:

$$I_{free}/C_{solvent} = -N_{solvent}J_{free}(C_{Li}/C_{solvent}) + J_{free}$$

Plots of $I_{free}/C_{solvent}$ against $C_{Li}/C_{solvent}$ exhibit a linear relationship with a slope of $-N_{solvent}J_{free}$ and an intercept of J_{free}, as shown in Figure 3c,d for the DMA-based electrolytes (Figure S3 for the DMF-based electrolytes). Then, dividing the slope by the intercept gives the value of $N_{solvent}$, yielding values of 2.2 ± 0.2 and 4.2 ± 0.7 for DMA-NO_3 and DMA-TFSI, respectively. Figure 3e illustrates the best estimation of the solvation structure for the two electrolytes in which the cations are solvated with two or four DMA molecules for DMA-NO_3 and DMA-TFSI, respectively. Because it has been reported that Li^+ preferably forms a tetrahedrally coordinated solvation structure, the $N_{solvent}$ value close to 4 verifies the validity of the Raman analysis. The lower solvation of DMA-NO_3 ($N_{solvent}$ = 2.2 ± 0.2) is due to the weaker dissociation of the $LiNO_3$ salt, which hampers tetrahedral coordination. We obtained the $N_{solvent}$ value of 4.1 ± 0.2 for DMF-TFSI (Figure S3), which is very close to the reported value with the same electrolyte (3.9 ± 0.1 by Fujii et al.[42]). Interestingly, no explicit peak decay was observed in I_{free} of DMF-NO_3 below 2.0 M concentration, indicating the weak solvation propensity of the solvent. I_{free} attenuates above 2.0 M, deriving 2.2 ± 1.2 as the $N_{solvent}$ for DMF-NO_3 (Figure S3). Although further analysis is needed to depict more accurate solvation structures, the Raman spectra clearly demonstrate that the NO_3-based electrolytes contain twice as much free solvent as the TFSI-based electrolytes. This results in solvent evaporation rates that are nearly twice as high for the NO_3-based electrolytes, as shown in Figure S4, which demonstrates the electrolyte solvent evaporation behavior from

https://doi.org/10.1021/acsaem.5c02972
ACS Appl. Energy Mater. 2026, 9, 827−841

a dummy stack cell, leading to an adverse impact on the battery performance, as discussed below.

3.2. Discharge Performance

The prepared electrolytes were combined with a CNT sheet cathode to assemble a stack-type LAB cell tested under dry-air containing 21% O_2. A highly porous CNT sheet cathode is essential for realizing atmospheric ORR, allowing continuous O_2 permeation across the whole cathode.[26] The stack cell configuration, in which the top surface of the cathode is covered by a current collector (Figure S1), was employed to secure the scalability of the cell capacity and current by stacking multiple electrodes. The cell inhales and exhales the O_2 gas through the cross section of the GDL. Because the amide-based electrolytes with low viscosity tend to have high volatility, the stack cell configuration is beneficial for suppressing solvent and maintaining electrode contact during battery testing.[43]

Parts a–c of Figure 4 show the discharge profiles of the LAB cells with DMA-NO_3 electrolytes of 0.25, 1.0, and 2.0 M. As expected, the cell with 1.0 M salt exhibited the best discharge performance, demonstrating stable voltage plateaus for up to 36 mA current rates (a current density of 18 mA cm^{-2} per electrode area) and delivering a capacity of 9.1 mAh (4.5 mAh cm^{-2}), thanks to the optimal balance of the high ionic conductivity and high fluidity. The 0.25 M electrolyte offered lower discharge performance with reduced voltages due to the scarcity of Li^+ carriers and the resulting decline in ionic conductivity. The discharge performance worsened in the 2.0 M electrolyte cell. Although the capacity at 4.0 mA rate was even higher than that of 0.25 or 1.0 M electrolyte cells, the discharge voltage was unstable and sharply dropped at 12 mA, resulting in a negligible discharge capacity. This should be ascribed to the excessively low ionic conductivity and diminished fluidity of the electrolyte. However, it should be mentioned that the discharge performance was much better than that of the cell with 1.0 M TEG-TFSI, which provided a negligible capacity above 4.0 mA rates (Figure S5). This insists the superiority of the low viscosity amide-based electrolytes as "true" LAB electrolytes capable of delivering high battery power and energy under ambient air. The salt concentration of 1.0 M was also superior for DMA-TFSI, DMF-NO_3, and DMF-TFSI electrolytes, compared to the 0.25 and 2.0 M electrolytes (the discharge profiles are shown in Figure S5). Among the 1.0 M electrolytes (Figure 4b,d–f), the DMF-NO_3 electrolyte (Figure 4e) exhibited an even higher current capability than DMA-NO_3, demonstrating an increased capacity of 5.8 mAh (2.9 mAh cm^{-2}) at a current of 36 mA (18 mA cm^{-2}). The current rate could be further increased to 46 mA (23 mA cm^{-2}), securing a capacity of 4.5 mAh (2.2 mAh cm^{-2}), or even up to 52 mA (26 mA cm^{-2}), to provide 1.7 mAh (0.9 mAh cm^{-2}) capacity, which is the highest current rate ever achieved under atmospheric O_2. The highest fluidity and improved ionic conductivity of DMF-NO_3 attained this ultrahigh current rate capability. While DMF-TFSI provided a discharge performance similar to that of DMA-NO_3, the DMA-TFSI cells fell behind, barely achieving stable discharge up to a 14 mA rate. This is likely due to the lowest fluidity among the 1.0 M electrolytes, which limited the smooth transport of the battery reactants.

To exemplify the new breed of battery power by LAB technology, gravimetric energy and power densities of the 1.0 M electrolyte cells were calculated, and the data were plotted in Figure 5b (Ragone plot). For the energy and power density calculations, the total mass of the cell materials (60.6 mg for the weight sum of carbon paper GDL, CNT sheet cathode, electrolyte, polyolefin separator, and Li foil anode, as illustrated in Figure 5a) was employed to best estimate the battery device

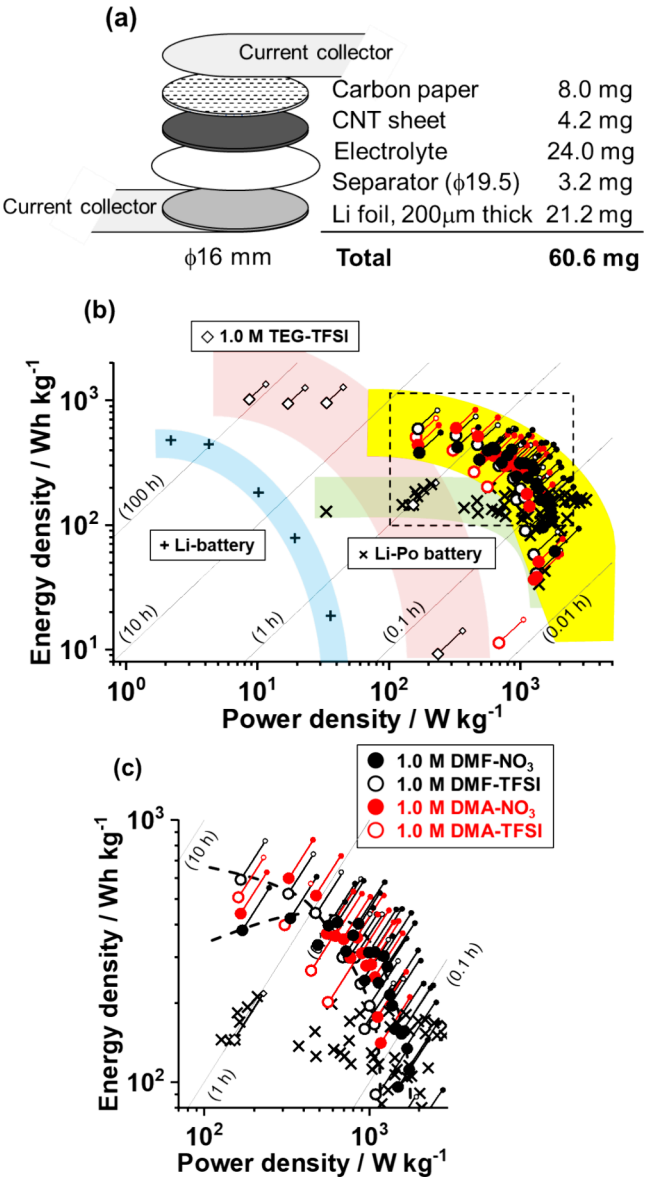

Figure 5. (a) Schematic illustration of the stack cell configuration for discharge experiments. The total weight of the cell materials was 60.6 mg for a 200-μm-thick Li foil cell, excluding the current collectors. (b) Energy density vs power density (Ragone plot). The pale-blue, green, red, and yellow areas indicate the trend of the data points for a lithium primary battery (+; the discharge data are shown in the Supporting Information), Li–Po battery (×, obtained by the survey report by Stux et al.,[44] with a 25 wt % deduction in battery weight to exclude the mass of the pouch and current collectors[45]), LAB cells with TEG-TFSI electrolyte (◇), and LAB cells with amide-based electrolytes, respectively. The reduced symbols in the upper right of each LAB cell plot represent the energy density and power density based on the virtual cell weight, assuming the minimum Li thickness. The gray diagonal lines indicate the discharge time. (c) Enlarged graph for the dotted square region in part b. The dotted lines indicate the trend of the data points for the cells with DMF-TFSI (○) and DMF-NO_3 (●) electrolytes.

https://doi.org/10.1021/acsaem.5c02972
ACS Appl. Energy Mater. 2026, 9, 827–841

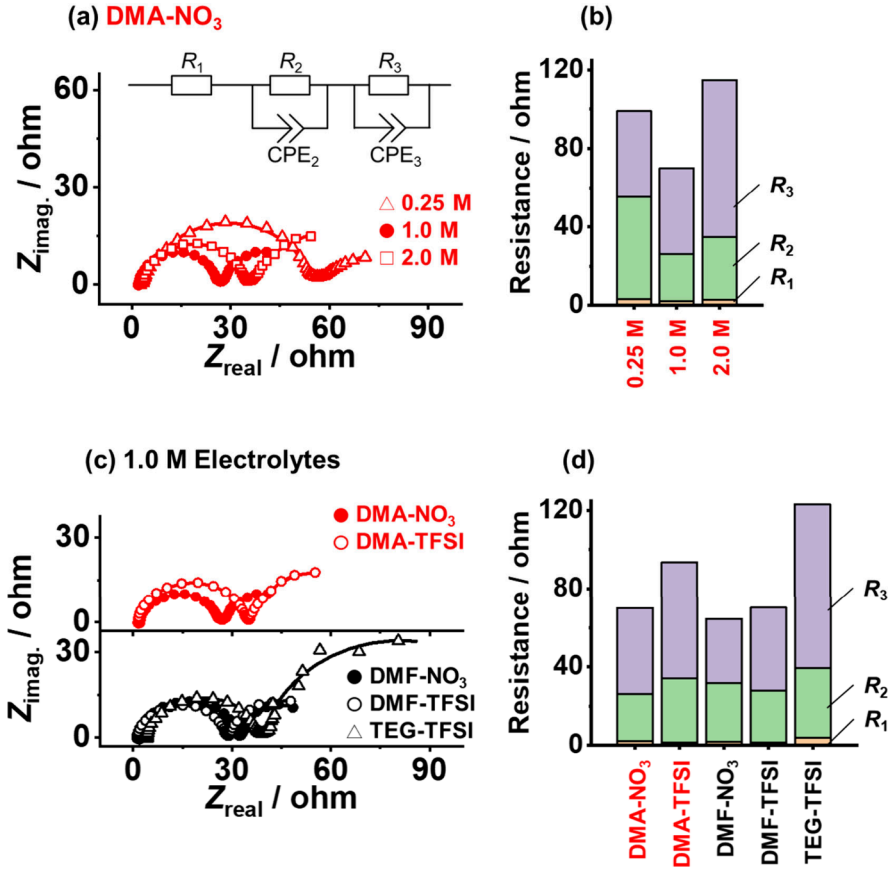

Figure 6. (a) Nyquist plots of the DMA-NO_3 electrolyte cells. The lines indicate the fitted curves for each plot using the electric circuit shown in the graph. (b) Stacked bar chart of the R_1, R_2, and R_3 values obtained by the impedance fitting shown in part a. (c) Nyquist plots of the 1.0 M DMA-based (top) and DMF-based electrolyte (bottom) cells. The lines indicate the fitted curves for each plot. (d) Stacked bar chart of the R_1, R_2, and R_3 values obtained by the impedance fitting. All of the R_1, R_2 and R_3 values with standard error and fit residuals are shown in the Supporting Information.

performance. To discuss the best possible energy/power densities achievable with the current cell configuration, the masses of the current collectors and the plates holding the cell configuration (Figure S1) were excluded. The tested cells use a 200 μm foil anode (a theoretical anode capacity of 82 mAh) to provide an adequate Li source for the cathode reaction, but this excess lithium mass undermines the energy and power density values. To demonstrate the best possible energy and power, values based on the virtual cell weight were also calculated and plotted with their reduced symbols. These values are determined by the weight of the thinnest lithium anode needed to deliver each cell capacity, with the other cell materials shown in Figure 5a (39–45 mg, depending on the cell capacity shown in Figure 4). Because the cells with a thinner foil anode (50 μm; a theoretical anode capacity of 21 mAh; Figure S6) exhibited the same discharge performance as that of the 200 μm anode cells, the lithium thickness barely affects discharge and rate capability as far as necessary and sufficient Li source was loaded. Therefore, the actual cell energy and power densities should lie on the projection lines between each symbol and its minified symbol. To compare the battery device performance, the energy and power densities of a lithium–polymer battery (Li–Po, ×), a small rechargeable battery device used in mobile phones, laptops, and multicopters (drones) based on LiB technology, were also plotted. From the Stux's survey report on the discharge power and energy of commercial Li–Po batteries,[44] the mass of the pouch pack and current collector foils (assumed to be 25 wt % of the cell pack[45]) were deducted to evaluate the energy and power densities based on the minimal cell components. The graph also includes the discharge power and energy of a lithium primary battery (Li-battery, +) widely used in small appliances, derived by discharging the commercial CR2032 cells (3.0 g) with a nominal voltage of 3.0 V and a nominal capacity of 240 mAh (Figure S6). The weight of the stainless CR2032 cases (1.7 g) was deducted to derive the energy/power densities based on 1.3 g of cell components (the total mass of the electrodes, separator, and electrolyte). The graph shows that the LAB cells with amide-based electrolytes perform far better than Li–Po and Li-battery devices, achieving 10 times the energy density of Li–Po and a 100 times the power of a Li battery, reaching into the territory of traditional combustion engines (>10^3 Wh kg^{-1} and >10^3 W kg^{-1}).[46] This results from the lightweight LAB cell materials and their enhanced current rate capability. Although previous studies have reported LAB cells with a high energy density (~10^3 Wh kg^{-1}), the slow ORR limited their power to below 100 W kg^{-1} even under pure O_2.[1−3] Achieving both high energy density beyond LiB and sufficient power output under atmospheric O_2 marks the emergence of a new class of battery devices based on LAB technology.

The low-viscosity (high-fluidity) amide-based electrolyte assumes a key role in the high-power capability of the cells. TEG-TFSI electrolyte cells (b, ◇) developed a relatively high

https://doi.org/10.1021/acsaem.5c02972
ACS Appl. Energy Mater. 2026, 9, 827−841

energy density of 960−1300 Wh kg^{-1} at 34−44 W kg^{-1} power, which surpasses that of previously reported LABs under pure O_2. However, the energy output dropped drastically and became negligible at a power condition of more than 300 W kg^{-1}, due to the severely limited O_2 transport in the high-viscosity electrolyte. Figure 5c shows the enlarged Ragone plot for the dotted square region of Figure 5b, revealing the power performance details of the amide-based electrolyte cells. DMF-NO_3 cells achieved the best power performance of all of the electrolytes, delivering 210 Wh kg^{-1} energy at 2200 W kg^{-1} power when 50 μm Li foil was used. These cells exceeded the high-energy criteria of 500 Wh kg^{-1} even at a power of 1000 W kg^{-1}. However, DMF-NO_3 cells demonstrated the lowest energy among other electrolyte cells at a low power of 170 W kg^{-1}. As with the DMA-NO_3 electrolyte cells, NO_3-based electrolytes exhibited declining energy when the power dropped below 300 W kg^{-1}, which was unlikely in the TFSI-based electrolytes. This behavior is evident from the discharge curves (Figure 4b,e), which showed reduced capacities at rates below 8.0 mA. The decreasing capacity at low current rates suggests progressive cell deterioration over time. The most plausible cause is evaporation of the electrolyte solvent, resulting in dry-out and a loss of cell contact. Due to the high vapor pressure of the amide solvents (1.8 mmHg for DMA and 3.5 mmHg for DMF), which are 10^3 times higher than that of TEG (1.5×10^{-3} mmHg),[43] the cells inevitably undergo electrolyte solvent evaporation immediately after cell assembly. This effect was more prominent in NO_3-based electrolytes due to the presence of greater amounts of free solvent molecules. Evaporation tests of dummy stack cells (Figure S4) suggest that NO_3-based electrolyte cells lose half their weight within 2−4 h after assembly, complicating long-term discharge lasting a few hours. In contrast, TFSI-based electrolytes containing fewer free solvent molecules better suppress solvent evaporation and maintain ion contact over longer durations, thereby enabling the extension of discharge and higher capacities at low current rates. This necessitates the need of rational electrolyte engineering tailored to the intended use of the battery device, including cell packaging designs that ensure smooth oxygen inhalation/exhalation while minimizing electrolyte evaporation. This is also an important issue in terms of reducing the release of harmful volatile organic compounds into the atmosphere. Because the evaporation of TEG-TFSI electrolytes is negligible compared to that of amide-based electrolytes, TEG-TFSI is the best option for LABs in extremely low power devices, providing the highest energy. Conversely, the plot suggests that low-viscosity amide-based electrolytes are most suitable for developing high-energy LAB devices for appliances with high power consumption, such as drones or electric vehicles.

EIS analysis was conducted to investigate the origin of the discharge overpotentials. Figure 6a shows the Nyquist plot for DMA-NO_3 electrolyte cells at concentrations of 0.25 1.0, and 2.0 M. The impedance spectra were recorded during galvanostatic discharge at 0.8 mA after 0.8 mAh discharge to remove the native skin layer on the Li anode and ensure minimal impedance for each cell throughout the discharge process. The graph clearly shows a semicircle at a frequency of 10^5−10^1 Hz, as well as an incomplete semicircle below 10^1 Hz. The 1.0 M electrolyte cell exhibited the lowest internal resistance. The spectra were fitted using the electrochemical circuit model shown in Figure 6a, in order to obtain three resistant components (R_1, R_2, and R_3), attributed to the high-frequency x-axis intercept, the middle-frequency semicircle, and the low-frequency semicircle, respectively. The results are shown in the bar chart in Figure 6b. The graph shows that the R_1 values, which correlate strongly with the electrolyte ionic conductivity, are less than 3.1 ohm for all cells and thus have little effect on the cell overpotential. R_2 and R_3, which are related to the Li anode and cathode reaction processes, respectively,[26] are the dominant resistance components for the cells. Of the three salt concentrations, the R_2 value for the 0.25 M cell was the highest, resulting from sluggish Li^+ dissolution from the Li anode. Meanwhile, R_3 was the highest for the 2.0 M cell and is attributed to the lowest fluidity (highest viscosity), which hampers O_2 dissolution and transport to the cathode surface. We previously demonstrated that cell discharge terminates along with the soaring proliferation of R_3, due to the failure of O_2 inhalation caused by accumulated Li_2O_2 deposition.[26] As discharge progresses, R_3 continuously increases, while R_1 and R_2 rather maintained their initial values (Figure S7 and Table S2). The increase in R_3 is more obvious in dry-air conditions than in pure O_2 stream. The increasing internal resistance during discharge results from pore blocking by accumulated Li_2O_2 on the cathode pores, which hinders O_2 transport. The low O_2 atmosphere makes O_2 transport more challenging. The increase in internal resistance due to the rise in R_3 suggests that O_2 transport dominates the magnitude of R_3. However, it should be noted that R_3 was not only correlated with electrolyte fluidity because the 1.0 M cell with middle fluidity exhibited a R_3 value similar to that of the 0.25 M cell having the lowest fluidity. Similar resistance behavior was also observed for DMA-TFSI, DMF-NO_3, and DMF-TFSI cells with varying salt concentrations (Figures S8 and S9). Further analysis of the impedance spectra is needed to identify the origin of R_2 and R_3; however, the spectra indicate that an optimal balance of electrolyte fluidity and Li^+ dissolution is required for a high power performance in LAB cells.

Figure 6c shows the Nyquist plots for the 1.0 M electrolyte cells. The R_1, R_2, and R_3 values obtained by impedance fitting are shown in Figure 6d. The graph reveals an exceptionally high R_3 value for the TEG-TFSI cell, which explains its low power capability. Among the amide-based electrolytes, the DMA-TFSI cell exhibited the highest R_2 and R_3 values, which compromised the high power performance of amide-based electrolytes. Although the total resistance values ($R_1 + R_2 + R_3$) were almost the same for the DMA-NO_3, DMF-NO_3, and DMF-TFSI cells at ∼60 ohm, the DMF-NO_3 cell exhibited a higher R_2 with a lower R_3 compared to the DMA-NO_3 and DMF-TFSI cells. While R_2 relates to the Li^+ dissolution of each electrolyte, the order of R_3 correlates well with the electrolyte fluidity among the 1.0 M electrolytes. Despite similar $R_1 + R_2 + R_3$ values, the relationship between the current rate (I) and cell voltage (V) of the LAB cells (I−V curves shown in Figure S10) revealed differential resistance, reducing the direct current resistance to 10 ohm for the DMF-NO_3 cells and 13 ohm for the DMA-NO_3 and DMF-TFSI cells. Nonohmic behavior is often observed in LAB cells with the heterogeneous cathode reaction, during which the pores clog and the surface passivated by the deposition of solid Li_2O_2.[47,48] The decreasing resistance in high current regions enabled a discharge current rate of up to 52 mA (26 mA cm^{-2}) for the DMF-NO_3 cells. This results from the electrolyte having the highest fluidity (lowest viscosity), which facilitates the smooth transport of the ions of O_2 and Li^+ across the whole cathode and ensures a homogeneous cathode reaction. Further engineering of the

https://doi.org/10.1021/acsaem.5c02972
ACS Appl. Energy Mater. 2026, 9, 827−841

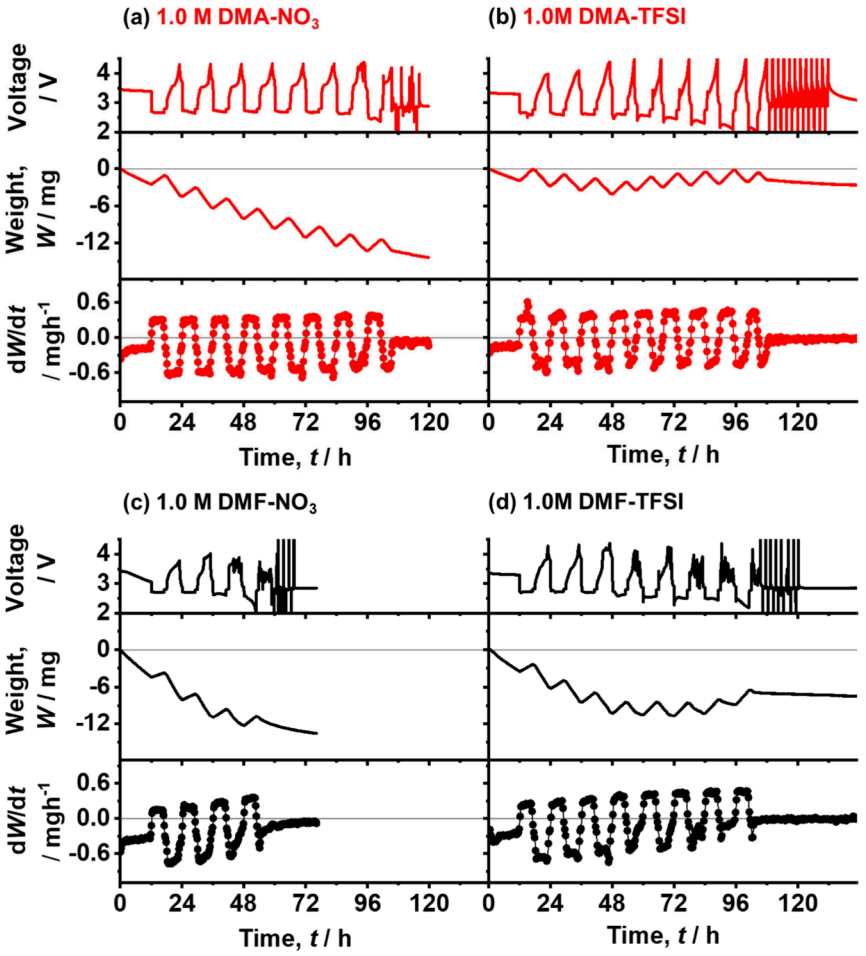

Figure 7. Voltage (top), cell weight (W, middle), and time derivative (dW/dt, bottom) profiles for the 1.0 M DMA-NO_3 (a), DMA-TFSI (b), DMF-NO_3 (c), and DMF-TFSI (d) cells. The discharge and charge cycle condition is 0.8 mA × 5 h.

electrolyte composition, based on a fundamental understanding of the internal battery resistance, will lead to the development of high-power battery devices with a high energy density, comparable to a combustion engine.

3.3. Cycle Performance

Even though the low-viscosity amide-based electrolytes demonstrate superior discharge power, it would be difficult to advance low-carbon economic growth and reduce greenhouse gases using LAB technology without sufficient rechargeability. To investigate the cycle performance of LAB cells with amide-based electrolytes, discharge−charge cycle tests were conducted under dry air. Figure 7 shows the voltage profiles of the LAB cells, including the cell weight (W) and its time derivative (dW/dt), which record the behavior of electrolyte evaporation simultaneously with the ORR/OER activity. Before the cycling test, an initial rest of 12 h was applied immediately after cell assembly. The W and dW/dt profiles during the rest period reveal a 90% reduction in the electrolyte evaporation compared to dummy stack cells (Figure S4), thanks to the cell configuration enclosed in a stainless-steel coin cell case (Figure S2). This enables long-term cycling of over 100 h. Even after cell packaging, the evaporation rates followed the same order: DMA-TFSI < DMA-NO_3, DMF-TFSI < DMF-NO_3. After the rest period, galvanostatic discharges and charges of 0.8 mA × 5 h (4.0 mAh) were applied. The repeating upward/downward shifts of ±0.48 mg h^{-1} in the dW/dt profiles during the 0.8 mA discharges−charges indicate that the cells undergo two-electron ORR/OER ($2e^-/O_2$) throughout their cycle life. This cycle condition provides an energy of approximately 200 Wh kg^{-1} at a power output of 40 W kg^{-1} with respect to the total mass of the cell materials. This relatively low power condition, compared to the cell's high power capability, was chosen to make the charge condition comply with the slow OER kinetics involving Li_2O_2 decomposition.

Figure 7 shows that the DMF-NO_3 cell has the poorest cyclability with only three cycle runs, despite its highest power capability. The W profile of the DMF-NO_3 cell (Figure 7c) demonstrates the greatest weight loss due to the highest evaporation behavior (−0.32 mg h^{-1} immediately before the first cycle run) among the amide-based electrolytes. The loss of the electrolyte solvent results in altered electrolyte properties and failed cell contact, triggering an inhomogeneous electrode reaction. By the end of the third charging, the DMF-NO_3 cell lost 12 mg of electrolyte solvent (40 wt % of the initial electrolyte amount), causing short circuit and charging failure, as evidenced by the unstable voltage profile. This resulted in the shortest cycle life for the DMF-NO_3 cell. Reduced electrolyte evaporation compared to the DMF-NO_3 cell (−0.25, −0.18, and −0.15 mg h^{-1} for DMF-TFSI, DMA-NO_3, and DMA-TFSI cells) provided better cyclability for other amide-based electrolyte cells, reaching up to 8 cycle runs. Despite having the same number of cycles, the high

https://doi.org/10.1021/acsaem.5c02972
ACS Appl. Energy Mater. 2026, 9, 827−841

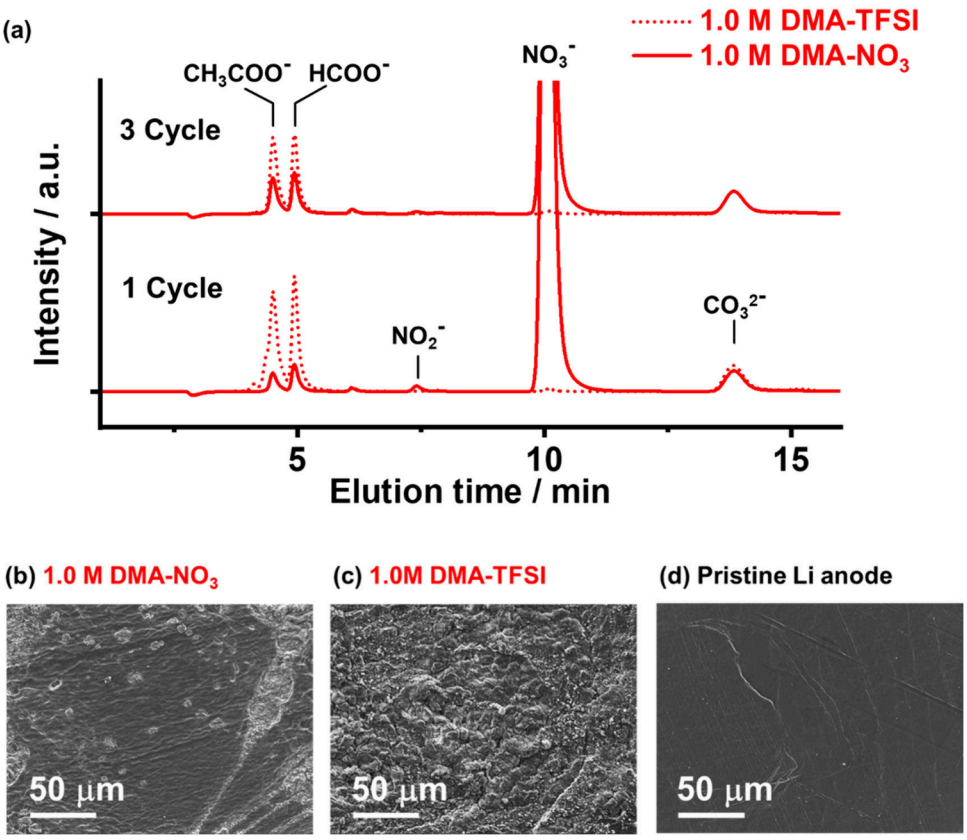

Figure 8. (a) Anion chromatography analysis of DMA-based electrolytes extracted from the cells after first discharge (bottom) and third charge (top). The chromatograph peaks at 4.5, 4.9, 7.4, 10.0, and 13.9 min are attributed to CH_3COO^-, $HCOO^-$, NO_2^-, NO_3^-, and CO_3^{2-} anions, respectively. The $TFSI^-$ anion was not detected due to the large anion size and thereby the too slow elution. SEM images of lithium metal anodes after first charge of DMA-NO_3 (b) and DMA-TFSI (c) electrolyte cells. The pristine lithium metal anode surface is shown in part d.

evaporation rate of the DMF-TFSI cell (−0.25 mg h^{-1}) resulted in a short circuit from the fourth charging. The lower evaporation of the DMA-NO_3 (Figure 7a) and DMA-TFSI (Figure 7b) cells completed their cycling without a short circuit, but the cells have different voltage and *W* profiles, suggesting different degradation mechanisms. Although the DMA-TFSI cell had the lowest evaporation rate (−0.15 mg h^{-1}), it suffered from declining discharge voltage along with cycle number, finally reaching the discharge cutoff (2.0 V) by the ninth cycle. Meanwhile, the DMA-NO_3 cell (−0.18 mg h^{-1}) maintained its 2.67 V discharge voltage until the seventh discharge; however, the cell experienced an abrupt drop in discharge voltage, reaching the cutoff at the ninth discharge. The sudden drop in the discharge voltage of the DMA-NO_3 cell should be attributed to electrolyte dry-out, as can be seen from the *W* profile showing a 12 mg weight loss (40 wt % electrolyte) by the eighth charge. On the contrary, the declining discharge voltage of the DMA-TFSI cell is assumed to result from the intrinsic instability of TFSI-based electrolytes, which was also observed for the DMF-TFSI cell (Figure 7d).

The electrochemical stability of DMA-based electrolytes was analyzed by using ion chromatography to investigate the mechanism of cell cycling deterioration. Figure 8a shows the anion chromatography of the DMA-NO_3 and DMA-TFSI electrolytes extracted from the polyolefin separator and the CNT cathode after the first and third charging. The graph shows the generation of impurities by oxidative decomposition of the electrolyte. The small NO_2^- peak (7.4 min) in the DMA-NO_3 electrolyte confirms the formation reaction of the NO_3^- anion SEI layer ($Li + 2NO_3^- \rightarrow LiO_2 + 2NO_2^-$). The generated NO_2^- anion reverts to NO_3^- in an oxygen atmosphere ($2NO_2^- + O_2 \rightarrow 2NO_3^-$).[11,32] However, the appearance of acetic (CH_3COO^-, 4.5 min) and formic ($HCOO^-$, 4.9 min) anion peaks, as well as the carbonic (CO_3^{2-}, 13.9 min) anion peak, clearly indicates DMA decomposition caused by an oxygen radical attack, which was more prominent for the DMA-TFSI electrolyte. This result aligns with a previous report by Kim et al., who revealed auto-oxidation of NMP-based electrolytes in the presence of lithium metal.[33] They also revealed that the NO_3^- anion in the NMP-based electrolyte provides anode protection by forming a protective layer, preventing autoxidation, and achieving stable cycling. Amides are not primarily suitable as LAB electrolyte solvents because of their narrow voltage window and high volatility compared to TEG. However, using $LiNO_3$ as a supporting salt makes amides an option for developing a promising LAB electrolyte by suppressing cell degradation. To observe the anode protection effect of $LiNO_3$, the lithium anodes of DMA-based electrolyte cells after the first charging were examined using SEM (Figure 8b,c), including pristine lithium anodes (Figure 8d). SEM images reveal a smoother, flatter surface morphology in the DMA-NO_3 cell (Figure 8b), with pits formed by Li dissolution that are incompletely filled by the subsequent Li deposition. The Li anode of the DMA-TFSI cell exhibited a rather granular uneven morphology, suggesting massive byproduct deposition by the electrolyte oxidation. The accumulation of these byproducts increases

https://doi.org/10.1021/acsaem.5c02972
ACS Appl. Energy Mater. 2026, 9, 827−841

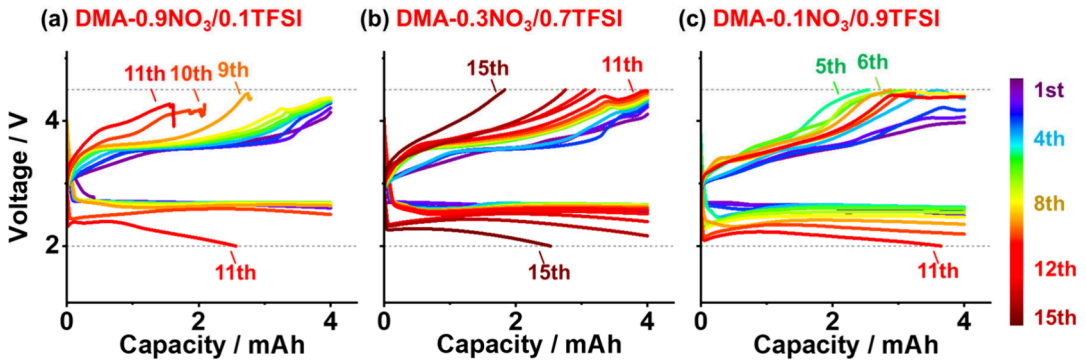

Figure 9. Discharge and charge curves of the LAB cells with mixed anion electrolytes of $0.9NO_3/0.1$TFSI (a), $0.3NO_3/0.7$TFSI (b), and $0.1NO_3/0.9$TFSI (c). The total salt concentration is 1.0 M. The discharge and charge cycle condition is 0.8 mA × 5 h. The dotted lines represent the discharge (2.0 V) and charge (4.5 V) cutoff voltages. The highest cycle numbers achieved by three sets of cells at each condition were plotted.

internal resistance, which gradually decreased the discharge voltage and limited cycle life. The DMA-NO_3 cell prevents electrolyte oxidation, successfully maintaining the discharge voltage. However, electrolyte evaporation limits the cycle life to no more than 8 cycles.

The above post-mortem analysis emphasizes the necessity of using $LiNO_3$ as a supporting salt in an amide-based electrolyte for a rechargeable LAB. Without the NO_3^- anion, stable cycling in LAB cells is difficult to achieve. However, NO_3-based electrolytes face fast solvent evaporation due to the weak solvation structure, resulting in an unsatisfactory cycle life. One way to break out of this dilemma is to mechanically suppress solvent volatilization. We have previously demonstrated that curtailing the ventilation path for O_2 gas exchange substantially enhances the cycle life of amide-based electrolyte cells.[43] Here, we introduce another strategy to improve the cycle life of NO_3^--based electrolyte cells: simply mix the $LiNO_3$ salt with the LiTFSI salt. Figure 9 shows the discharge and charge curves of DMA-based electrolyte cells with a 1.0 M Li^+ concentration and mixed anions of three compositions. The cycling conditions are the same as those in Figure 8. Cells with $0.9NO_3/0.1$TFSI (Figure 9a) and $0.1NO_3/0.9$TFSI (Figure 9c) showed minor improvement in cyclability, displaying voltage behaviors similar to those of DMA-NO_3 and DMA-TFSI cells, respectively. Adding a small amount of the TFSI anion to DMA-NO_3 ($0.9NO_3/0.1$TFSI) extends the cycle life by reducing DMA volatilization. Meanwhile, adding the NO_3 anion to the DMA-TFSI ($0.1NO_3/0.9$TFSI) protects the lithium anode by reducing DMA solvent decomposition, thereby prolonging the cycle life. The best cyclability was found in a $0.3NO_3/0.7$TFSI anion ratio cell (Figure 9b), achieving 14 cycle runs with a discharge voltage of >2.5 V up to the 13th discharge. Interestingly, the weight change measurement of the $0.3NO_3/0.7$TFSI cell (Figure S11) revealed more suppressed electrolyte evaporation (−0.11 mg h^{-1}), whereas that of the DMA-TFSI cell was −0.15 mg h^{-1}. Competitive solvent solvation of the two anions may result in reduced electrolyte evaporation in the $0.3NO_3/0.7$TFSI cell. Previous papers have reported over 100 cycle runs in LAB cells under a pure O_2 atmosphere ($Li-O_2$),[36−38] but achieving a high energy density beyond LiB technology (100−200 Wh kg^{-1}) by capacities of less than 1.0 mAh cm^{-2} would be difficult. Furthermore, it would be impractical to obtain a high energy density from the $Li-O_2$ system coming with an O_2 gas cylinder and gastight tubing. An Li−air system that uses atmospheric O_2 for its discharge−charge can produce only high-energy-density batteries, which are the "true" LABs. The cycle condition in this study that provides 200 Wh kg^{-1} energy in dry air is much closer to that of a practical LAB system. Although 14 cycle runs still fail to demonstrate sufficient rechargeability for a secondary battery, further engineering of the electrolytes and cell configuration to suppress electrolyte evaporation and decomposition will further improve the cycle performance.

Finally, we discuss the differences between the two systems: "$Li-O_2$" and "Li−air". The increased power and energy of the "Li−air" system pave the way for the development of "true" LAB devices that can operate under atmospheric O_2. However, this raises an important question: Can the accumulated knowledge from the $Li-O_2$ system simply be applied to the development of "true" LABs? Figure 10a compares the voltage and dW/dt profiles of the first three cycle runs of DMA-NO_3 cells tested under dry-air (Li−air) and pure O_2 gas flow ($Li-O_2$). The complete discharge and charge curves shown in Figure S12 demonstrate similar cycle numbers (8−9) for both systems. Thus, the low O_2 gas atmosphere (~21%) does not significantly deteriorate the cycle performance of the amide-based electrolyte cells. Because the discharge voltage of the Li−air system was slightly lower than that of the $Li-O_2$ system (2.67 V vs 2.74 V at the end of the first discharge), the 21% O_2 gas results in less than a 3% decrease in energy and power capability. Because the dW/dt curves trace the same $2e^-/O_2$ ORR/OER profile, the Li−air and $Li-O_2$ systems share the same electrochemistry. However, the $Li-O_2$ system exhibited a rapid increase in charging voltage, faster than that of the Li−air system, indicating potentially faster degradation. Anion chromatography of the DMA-NO_3 electrolytes after the first and third charges revealed the generation of degradants that were more prominent in the $Li-O_2$ system. While the peak intensities for the CH_3COO^- and CO_3^{2-} anions were nearly identical for the two systems, $Li-O_2$ exhibited a peak intensity of the $HCOO^-$ anion twice as high as that of the Li−air system. There was also an unknown anion (*, 6.2 min) that could not be identified at this time. This suggests more severe electrolyte decomposition in the $Li-O_2$ system by the ~5 times higher O_2 concentration. While the higher O_2 concentration is beneficial for boosting battery energy and power, it adversely affects cycle life due to the higher probability of oxygen radical attacks. In addition, the difference in the O_2 partial pressure alters the Li_2O_2 discharge product. Despite having the same discharge capacity, the XRD spectra of the cathodes after the first discharge reveal broader, less

https://doi.org/10.1021/acsaem.5c02972
ACS Appl. Energy Mater. 2026, 9, 827−841

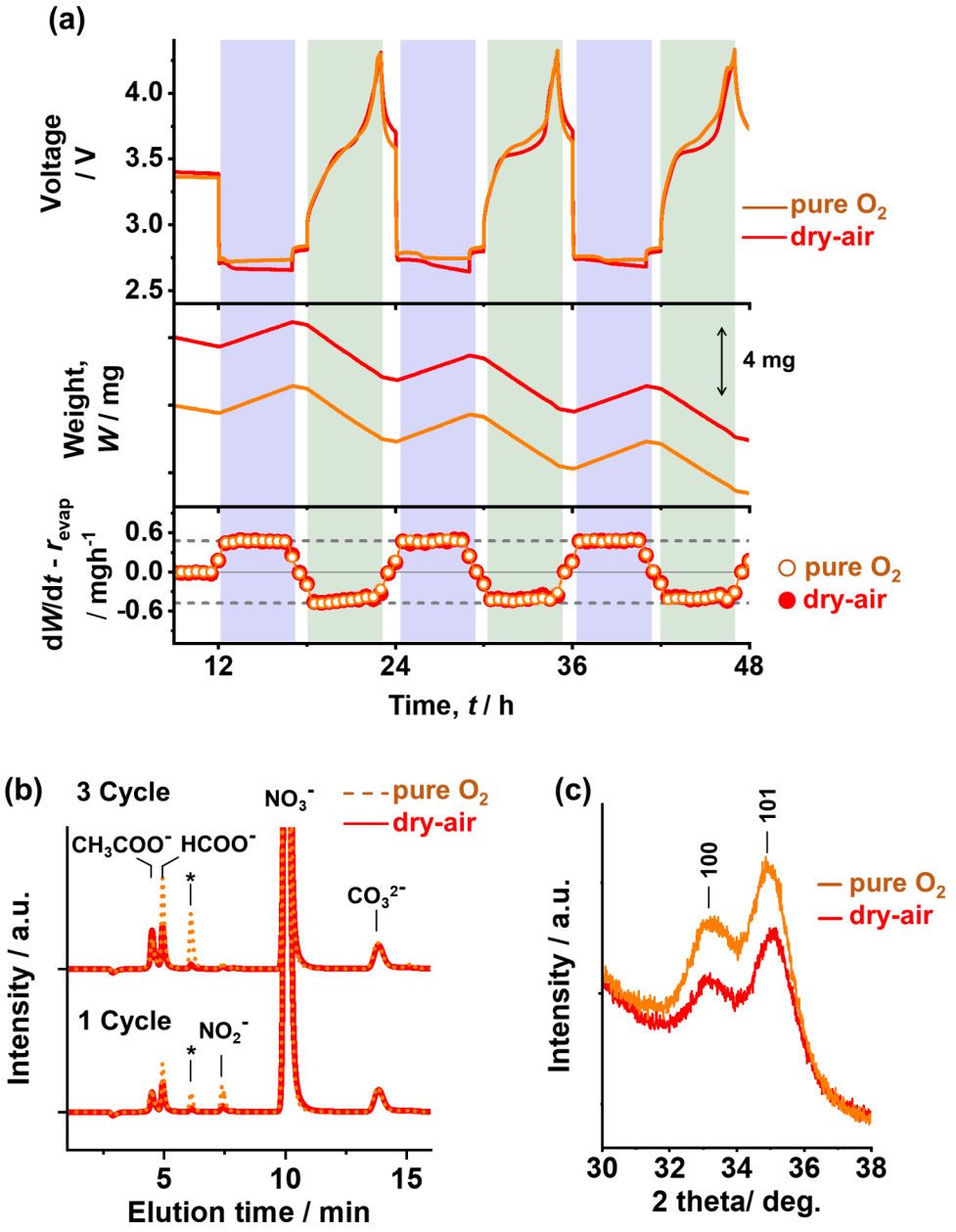

Figure 10. (a) Voltage (top), cell weight (W, middle), and time derivative (dW/dt, bottom) profiles for the 1.0 M DMA-NO_3 cells tested under dry air (red) and pure O_2 gas (orange). The pale-blue and green squares show the regions during discharge and charge, respectively. The solvent evaporation rate (r_{evap}) was deducted from the dW/dt profiles. The dotted gray lines indicate $2e^-/O_2$ ORR/OER (± 0.48 mg h^{-1} at 0.8 mA). (b) Anion chromatography analysis of the DMA-based electrolytes extracted from the cells after the first (bottom) and third (top) charges. (c) XRD spectra of the CNT sheet cathodes extracted from the cells after 8 mAh discharge. The numbers in the graph indicate the Miller indices for the Li_2O_2 crystal diffraction.

intense peaks of the Li_2O_2 100 and 101 reflections in the Li–air system, indicating a more amorphous Li_2O_2. The decrease in Li_2O_2 crystallinity resembles the Li_2O_2 plating via a surface O_2 reduction pathway ($Li^+ + O_2 + e^- \rightarrow LiO_2$ and $Li^+ + LiO_2 + e^- \rightarrow Li_2O_2$) rather than the disproportionation reaction of the LiO_2 intermediate ($Li^+ + O_2 + e^- \rightarrow LiO_2$ and $2LiO_2 \rightarrow Li_2O_2 + O_2$).[47,49] At the same discharge rate, the low O_2 concentration likely shifted the ORR process toward surface reduction, resulting in the growth of amorphous, film-like Li_2O_2, which is easier to decompose due to the better electronic conductivity and closer contact with the cathode surface.[50] This process leads to a suppressed increase in the charging voltage in Li–air compared to that in Li–O_2. These results suggest that while the fundamental electrochemistry is the same for both systems, the thermodynamic behavior inside the cells is completely different. Therefore, the systems must be clearly distinguished and discussed separately. Due to the difficulty of deriving sufficient power and energy in atmospheric O_2, most previous LAB studies have focused on the Li–O_2 system rather than the Li–air system. However, achieving high power and energy in dry air using a low-viscosity amide-based electrolyte and porous cathode encourages the exploration of low O_2 electrochemistry for "true" LABs. Such studies are just the beginning.

https://doi.org/10.1021/acsaem.5c02972
ACS Appl. Energy Mater. 2026, 9, 827–841

4. CONCLUSIONS

To demonstrate the high power and energy capabilities of LABs under atmospheric O_2, this study investigated the discharge and cycle performances of stack-type LAB cells with a low-viscosity amide-based electrolyte in dry air. This solvent enables high-current-rate discharge in LABs by facilitating the smooth supply of reactants Li^+ and O_2, surpassing traditional TEG-based electrolytes. Among the examined amide-based electrolytes, DMF-NO_3 with the lowest viscosity and highest fluidity, achieved the best power performance, delivering 2200 W kg^{-1} of power and 210 Wh kg^{-1} of energy. Conversely, the discharge−charge cycle test revealed that DMA-based electrolytes exhibit the best rechargeability due to reduced solvent evaporation. Optimizing the composition of the NO_3^- and $TFSI^-$ anions suppressed solvent volatilization and electrolyte degradation, enabling 14 cycle runs providing 200 Wh kg^{-1} of energy. The electrolyte viscosity, ion conductivity, and solvent volatility are highly correlated to the solvation structure, as analyzed by Raman spectroscopy. The battery performance demonstrated here suggests the emergence of a new battery device that surpasses LiB and Li−primary battery technologies in both power and energy storage, although acquiring good rechargeability remains a critical breakthrough. This breakthrough would not just be limited to achieving tolerable cyclability through battery charging; another option is assembling a low-cost battery device using environmentally benign materials. Although DMF and DMA electrolytes can be hazardous air pollutants if evaporated into the environment, the strategy of using a low-viscosity electrolyte to achieve a high-energy and high-power performance will lead to the development of lower toxic alternatives. Because LAB electrodes are composed purely of carbon and lithium and contain no precious or poisonous metals, LABs also demonstrate superiority in terms of material cost and recyclability. Good rechargeability also enables the low-cost recycling of lithium resources from used batteries. Further investigation is required to understand the effects of gas impurities, such as atmospheric CO_2 and humidity. Pursuing a high-power and high-energy performance through low-cost battery assembly technology will ultimately lead to the realization of a "true" LAB capable of use in ambient air.

■ ASSOCIATED CONTENT

Supporting Information

The Supporting Information is available free of charge at https://pubs.acs.org/doi/10.1021/acsaem.5c02972.

Data table for electrolyte ionic conductivity and viscosity, schematic illustrations of cell configurations, Raman spectra of the DMF-based electrolytes, electrolyte evaporation behavior from the dummy stack cell, additional discharge curve profiles, EIS fitting result, and *I*−*V* curves (PDF)

■ AUTHOR INFORMATION

Corresponding Author

Akihiro Nomura − *Research Center for Energy and Environmental Materials, National Institute for Materials Science (NIMS), Ibaraki 305-0044, Japan;* orcid.org/0000-0001-5012-4739; Email: nomura.akihiro@nims.go.jp

Authors

Shota Azuma − *Research Center for Energy and Environmental Materials, National Institute for Materials Science (NIMS), Ibaraki 305-0044, Japan; Department of Science and Technology, Faculty of Science and Technology, Seikei University, Tokyo 180-8633, Japan; National Institute of Technology, Tokyo College, Tokyo 193-0997, Japan*

Fumisato Ozawa − *Department of Science and Technology, Faculty of Science and Technology, Seikei University, Tokyo 180-8633, Japan;* orcid.org/0009-0008-7214-0885

Morihiro Saito − *Department of Science and Technology, Faculty of Science and Technology, Seikei University, Tokyo 180-8633, Japan;* orcid.org/0000-0001-7062-8336

Complete contact information is available at: https://pubs.acs.org/10.1021/acsaem.5c02972

Author Contributions

A.N.: conceptualization, investigation, methodology, data curation, formal analysis, funding acquisition, writing—original draft, and writing—review and editing. S.A.: data curation and writing——review and editing. F.O.: writing—review and editing. M.S.: writing—review and editing and funding acquisition.

Funding

This study was supported by the JST Adaptable and Seamless Technology Transfer Program through Target-Driven Research and Development (A-STEP; Grant JPMJTM22AQ), JSPS KAKENHI (Grants 24K08154 and 24K08585), and Japan Keirin Autorace Foundation (Grant 2024M-380). This work was also supported by the NIMS Joint Research Hub Program.

Notes

The authors declare no competing financial interest.

■ ACKNOWLEDGMENTS

The authors thank Hisae Uematsu for technical assistance. Material characterization and cell assembly were performed using the NIMS Battery Research Platform, with usage fees.

■ REFERENCES

(1) Park, J. O.; Kim, M.; Kim, J. H.; Choi, K. H.; Lee, H. C.; Choi, W.; Ma, S. B.; Im, D. A 1000 Wh kg^{-1} Li-Air battery: Cell design and performance. *J. Power Sources* **2019**, *419*, 112−118.

(2) Zhao, S. Q.; Zhang, L.; Zhang, G. N.; Sun, H. B.; Yang, J. Y.; Lu, S. G. Failure analysis of pouch-type Li-O_2 batteries with superior energy density. *J. Energy Chem.* **2020**, *45*, 74−82.

(3) Wen, Z.; Liu, Y.; Li, K.; Yang, S.; Zhou, H.; He, P. Boosting the Li-O_2 pouch cell beyond 860 Wh kg^{-1} by an O_2-enriched localized high-concentration electrolyte. *Natl. Sci. Rev.* **2025**, DOI: 10.1093/nsr/nwaf059.

(4) Kwon, H. J.; Lee, H. C.; Ko, J.; Jung, I. S.; Lee, H. C.; Lee, H.; Kim, M.; Lee, D. J.; Kim, H.; Kim, T. Y.; et al. Effects of oxygen partial pressure on Li-air battery performance. *J. Power Sources* **2017**, *364*, 280−287.

(5) Yao, W.; Yuan, Y.; Tan, G.; Liu, C.; Cheng, M.; Yurkiv, V.; Bi, X.; Long, F.; Friedrich, C. R.; Mashayek, F.; et al. Tuning Li_2O_2 Formation Routes by Facet Engineering of MnO_2 Cathode Catalysts. *J. Am. Chem. Soc.* **2019**, *141*, 12832−12838.

(6) Li, Y.; Qiu, Y.; Wang, Y.; Wang, L.; Lv, Q. Atomically Asymmetrical Ruthenium−Oxygen−Cobalt Sites Accelerate Oxygen Redox and Suppress Side Reactions for Stable Lithium−Oxygen Batteries. *ACS Nano* **2025**, *19*, 32643.

(7) Liang, Z. J.; Lu, Y. C. Critical Role of Redox Mediator in Suppressing Charging Instabilities of Lithium-Oxygen Batteries. *J. Am. Chem. Soc.* **2016**, *138*, 7574−7583.
(8) Xin, X.; Ito, K.; Kubo, Y. Highly Efficient Br^-/NO^{3-} Dual-Anion Electrolyte for Suppressing Charging Instabilities of Li-O_2 Batteries. *ACS Appl. Mater. Interfaces* **2017**, *9*, 25976−25984.
(9) Azuma, S.; Sano, M.; Moro, I.; Ozawa, F.; Saito, M.; Nomura, A. Redox Mediator-Coated Air-Electrodes for High-Capacity Cycle Operation of Lithium−Air Batteries. *J. Phys. Chem. C* **2023**, *127*, 7087−7094.
(10) Azuma, S.; Moro, I.; Sano, M.; Ozawa, F.; Saito, M.; Nomura, A. Mechanistic Analysis of Lithium-Air Battery with Organic Redox Mediator-Coated Air-Electrode. *J. Electrochem. Soc.* **2024**, *171*, 100511.
(11) Azuma, S.; Sano, M.; Moro, I.; Ozawa, F.; Saito, M.; Nomura, A. Improving the cycling performance of lithium-air batteries using a nitrite salt electrolyte. *Electrochim. Acta* **2024**, *489*, 144261.
(12) Wan, H.; Bai, Q.; Peng, Z.; Mao, Y.; Liu, Z.; He, H.; Wang, D.; Xie, J.; Wu, G. A high power Li−air battery enabled by a fluorocarbon additive. *J. Mater. Chem. A* **2017**, *5*, 24617−24620.
(13) Wijaya, O.; Rinaldi, A.; Younesi, R.; Yazami, R. The Origin of Li-O2Battery Performance Enhancement Using Fluorocarbon Additive. *J. Electrochem. Soc.* **2016**, *163*, A2660−A2664.
(14) Wijaya, O.; Hartmann, P.; Younesi, R.; Markovits, I. I. E.; Rinaldi, A.; Janek, J.; Yazami, R. A gamma fluorinated ether as an additive for enhanced oxygen activity in Li−O_2 batteries. *J. Mater. Chem. A* **2015**, *3*, 19061−19067.
(15) Hayashi, M.; Minowa, H.; Takahashi, M.; Shodai, T. Surface Properties and Electrochemical Performance of Carbon Materials for Air Electrodes of Lithium-Air Batteries. *Electrochemistry* **2010**, *78*, 325−328.
(16) Ma, S. B.; Lee, D. J.; Roev, V.; Im, D.; Doo, S. G. Effect of porosity on electrochemical properties of carbon materials as cathode for lithium-oxygen battery. *J. Power Sources* **2013**, *244*, 494−498.
(17) Ding, N.; Chien, S. W.; Hor, T. S. A.; Lum, R.; Zong, Y.; Liu, Z. Influence of carbon pore size on the discharge capacity of Li−O_2 batteries. *J. Mater. Chem. A* **2014**, *2* (31), 12433−12441.
(18) Park, J.; Jeong, J.; Lee, S.; Jo, C.; Lee, J. Effect of Mesoporous Structured Cathode Materials on Charging Potentials and Rate Capability of Lithium−Oxygen Batteries. *ChemSusChem* **2015**, *8*, 3146−3152.
(19) Sakai, K.; Iwamura, S.; Mukai, S. R. Influence of the Porous Structure of the Cathode on the Discharge Capacity of Lithium-Air Batteries. *J. Electrochem. Soc.* **2017**, *164*, A3075−A3080.
(20) Nomura, A.; Ito, K.; Kubo, Y. CNT Sheet Air Electrode for the Development of Ultra-High Cell Capacity in Lithium-Air Batteries. *Sci. Rep.* **2017**, *7*, 45596.
(21) Li, J.; Zhang, Y.; Zhou, W.; Nie, H.; Zhang, H. A hierarchically honeycomb-like carbon via one-step surface and pore adjustment with superior capacity for lithium−oxygen batteries. *J. Power Sources* **2014**, *262*, 29−35.
(22) Sakai, K.; Iwamura, S.; Sumida, R.; Ogino, I.; Mukai, S. R. Carbon Paper with a High Surface Area Prepared from Carbon Nanofibers Obtained through the Liquid Pulse Injection Technique. *ACS Omega* **2018**, *3*, 691−697.
(23) Dutta, A.; Ito, K.; Kubo, Y. Establishing the criteria and strategies to achieve high power during discharge of a Li-air battery. *J. Mater. Chem. A* **2019**, *7*, 23199−23207.
(24) Ushijima, K.; Iwamura, S.; Mukai, S. R. Simple and Cost-Effective Method to Increase the Capacity of Carbon Nanotube Sheet Cathodes for Lithium-Air Batteries. *ACS Appl. Energy Mater.* **2020**, *3*, 6915−6921.
(25) Nomura, A.; Mizuki, E.; Ito, K.; Kubo, Y.; Yamagishi, T.; Uejima, M. Highly-porous Super-Growth carbon nanotube sheet cathode develops high-power Lithium-Air Batteries. *Electrochim. Acta* **2021**, *400*, 139415.
(26) Nomura, A.; Azuma, S.; Ozawa, F.; Saito, M. Highly porous carbon nanotube air-electrode combined with low-viscosity amide-based electrolyte enabling high-power, high-energy lithium-air batteries. *J. Power Sources* **2025**, *633*, 236426.
(27) Freunberger, S. A.; Chen, Y. H.; Drewett, N. E.; Hardwick, L. J.; Barde, F.; Bruce, P. G. The Lithium-Oxygen Battery with Ether-Based Electrolytes. *Angew. Chem., Int. Ed.* **2011**, *50*, 8609−8613.
(28) Chen, Y.; Freunberger, S. A.; Peng, Z.; Bardé, F.; Bruce, P. G. Li−O_2 Battery with a Dimethylformamide Electrolyte. *J. Am. Chem. Soc.* **2012**, *134*, 7952−7957.
(29) Wang, H.; Xie, K.; Wang, L.; Han, Y. *N*-methyl-2-pyrrolidone as a solvent for the non-aqueous electrolyte of rechargeable Li-air batteries. *J. Power Sources* **2012**, *219*, 263−271.
(30) Walker, W.; Giordani, V.; Uddin, J.; Bryantsev, V. S.; Chase, G. V.; Addison, D. A Rechargeable Li−O_2 Battery Using a Lithium Nitrate/*N,N*-Dimethylacetamide Electrolyte. *J. Am. Chem. Soc.* **2013**, *135*, 2076−2079.
(31) Nomura, A.; Ito, K.; Yu, D. Y. W.; Kubo, Y. Gravimetric analysis of lithium-air batteries during discharge/charge cycles. *J. Power Sources* **2024**, *592*, 233924.
(32) Uddin, J.; Bryantsev, V. S.; Giordani, V.; Walker, W.; Chase, G. V.; Addison, D. Lithium Nitrate As Regenerable SEI Stabilizing Agent for Rechargeable Li/O2 Batteries. *J. Phys. Chem. Lett.* **2013**, *4*, 3760−3765.
(33) Kim, D. W.; Lee, D. H.; Ahn, S. M.; Kim, D. Y.; Suk, J.; Choi, D. H.; Kang, Y. Autoxidation in amide-based electrolyte and its suppression for enhanced oxygen efficiency and cycle performance in non-aqueous lithium oxygen battery. *J. Power Sources* **2017**, *347*, 186−192.
(34) Chen, J.; Chen, C.; Huang, T.; Yu, A. LiTFSI Concentration Optimization in TEGDME Solvent for Lithium−Oxygen Batteries. *ACS Omega* **2019**, *4*, 20708−20714.
(35) Xu, W.; Cooper, E. I.; Angell, C. A. Ionic Liquids: Ion Mobilities, Glass Temperatures, and Fragilities. *J. Phys. Chem. B* **2003**, *107*, 6170−6178.
(36) Yuan, H.; Wu, H.; Xia, P.; Zeng, Y.; Tang, M.; Che, Y.; Yang, X.; Han, Z.; Yuan, Y.; Dong, Y. Porous Core−Shell Co_3O_4@$CuCo_2O_4$ Derived from Metal−Organic Frameworks as the Cathode Material for Lithium−Oxygen Batteries. *Langmuir* **2025**, *41*, 20967−20974.
(37) Park, S.-J.; Jang, J.-S.; Park, D.-H.; Kim, J.-H.; Lee, G.-I.; Kim, M.-J.; Jang, S.-Y.; Park, K.-W. Enhancing Oxygen Redox Reversibility in Li−O_2 Batteries via Bimetallic Phosphide Catalysts with Tailored Surface Morphology and Electronic Structure. *Small* **2025**, *21*, No. e05547.
(38) Zhang, Q.; Huang, Y.; Hu, H.; Ma, C.; Zhong, Y.; Wu, P.; Lv, W.; Li, F.; Liu, X. In situ fabrication of ether-in-gel electrolyte enables long-cycle Li−air batteries over a wide temperature range. *eScience* **2025**, 100457.
(39) Spohn, P. D.; Brill, T. B. Raman spectroscopy of the species in concentrated aqueous solutions of zinc nitrate, calcium nitrate, cadmium nitrate, lithium nitrate and sodium nitrate up to 450 °C and 30 MPa. *J. Phys. Chem.* **1989**, *93*, 6224−6231.
(40) Castriota, M.; Caruso, T.; Agostino, R. G.; Cazzanelli, E.; Henderson, W. A.; Passerini, S. Raman Investigation of the Ionic Liquid *N*-Methyl-*N*-propylpyrrolidinium Bis-(trifluoromethanesulfonyl)imide and Its Mixture with $LiN(SO_2CF_3)_2$. *J. Phys. Chem. A* **2005**, *109*, 92−96.
(41) Umebayashi, Y.; Matsumoto, K.; Mekata, I.; Ishiguro, S. Solvation structure of lanthanide(iii) ions in solvent mixtures of *N,N*-dimethylformamide and *N,N*-dimethylacetamide studied by titration Raman spectroscopy. *Phys. Chem. Chem. Phys.* **2002**, *4*, 5599−5605.
(42) Fujii, K.; Wakamatsu, H.; Todorov, Y.; Yoshimoto, N.; Morita, M. Structural and Electrochemical Properties of Li Ion Solvation Complexes in the Salt-Concentrated Electrolytes Using an Aprotic Donor Solvent, N,N-Dimethylformamide. *J. Phys. Chem. C* **2016**, *120*, 17196−17204.
(43) Nomura, A.; Azuma, S.; Ozawa, F.; Saito, M. Rational Choice of Amide-Based Electrolytes Toward High-Power Rechargeable Lithium-Air Batteries. *Energy Technol.* **2025**, *13*, 2500556.

https://doi.org/10.1021/acsaem.5c02972
ACS Appl. Energy Mater. 2026, 9, 827−841

(44) Arnold, M. S.; Karen, S.-L. *Survey of Commercial Small Lithium Polymer Batteries*; Naval Research Laboratory, 2007; NRL/MR/6110-07-9073. https://apps.dtic.mil/sti/citations/ADA472272.
(45) Sommerville, R.; Zhu, P.; Rajaeifar, M.; Heidrich, O.; Goodship, V.; Kendrick, E. A qualitative assessment of lithium ion battery recycling process. *Resour. Conserv. Recy.* **2021**, *165*, 105219.
(46) Zhou, R.; Wei, S.; Liu, Y.; Gao, N.; Wang, G.; Lian, J.; Jiang, Q. Charge Storage by Electrochemical Reaction of Water Bilayers Absorbed on MoS2Monolayers. *Sci. Rep.* **2019**, *9*, 3980.
(47) Wang, L.; Noguchi, H. Oxygen Reduction Reaction Mechanism in Highly Concentrated Lithium Nitrate-Dimethyl Sulfoxide: Effect of Lithium Nitrate Concentration. *J. Phys. Chem. C* **2022**, *126*, 11457−11467.
(48) Zhang, Z.; Xiao, X.; Yan, A.; Sun, K.; Yu, J.; Tan, P. Breaking the capacity bottleneck of lithium-oxygen batteries through reconceptualizing transport and nucleation kinetics. *Nat. Commun.* **2024**, *15* (1), 9952.
(49) Dutta, A.; Ito, K.; Nomura, A.; Kubo, Y. Quantitative Delineation of the Low Energy Decomposition Pathway for Lithium Peroxide in Lithium-Oxygen Battery. *Adv. Sci.* **2020**, *7*. DOI: 10.1002/advs.202001660.
(50) Plunkett, S. T.; Wang, H.-H.; Park, S. H.; Lee, Y. J.; Cabana, J.; Amine, K.; Al-Hallaj, S.; Chaplin, B. P.; Curtiss, L. A. Charge Transport Properties of Lithium Superoxide in Li−O_2 Batteries. *ACS Appl. Energy Mater.* **2020**, *3*, 12575−12583.

https://doi.org/10.1021/acsaem.5c02972
ACS Appl. Energy Mater. 2026, 9, 827−841